# Augmented Experiment in Material Engineering Using Machine Learning

**Aomar Osmani**[1], **Massinissa Hamidi**[1], **Salah Bouhouche**[2]
[1] Laboratoire LIPN-UMR CNRS 7030, Univ. Sorbonne Paris Nord
[2] Industrial Technologies Research Center, CRTI-DTSI
{ao, hamidi}@lipn.univ-paris13.fr

## Abstract

The synthesis of materials using the principle of thermogravimetric analysis to discover new anticorrosive paints requires several costly experiments. This paper presents an approach combining empirical data and domain analytical models to reduce the number of real experiments required to obtain the desired synthesis. The main idea is to predict the behavior of the synthesis of two materials with well-defined mass proportions as a function of temperature. As no exact equational model exists to predict the new material, we integrate a machine learning approach circumscribed by existing domain analytical models such as heating equation in order to derive a generative model of augmented experiments. Extensive empirical evaluation shows that using machine learning approach guided by analytic models, it is possible to substantially reduce the number of needed physical experiments without losing the approximation quality. [1]

## Introduction

Many important engineering processes do not have an explicit and complete analytic description of the objective function and consider the transformation processes as black-box functions which result, for example, from experiments or non-linear systems (Biegler, Lang, and Lin 2014). It is particularly the case for material design industry, where the core function is to accelerate the synthesis of new materials with good properties (Aykol et al. 2019; Severson et al. 2019; Tabor et al. 2018). To this end, kinetics and thermodynamics measurements of the thermal degradation for non-charring polymers are performed (Li and Stoliarov 2013). Despite the existence of several theoretical simulation models, it remains difficult to design rigorous physical models including the information on the mechanisms of reactions in all the cases with expensive and time-consuming experiments (Zander, Dittmeyer, and Wagenhuber 1999).

This paper deals with combining known theoretical models on the pigments and dyes industry, particularly in the synthesis of an anticorrosive paint, and machine learning techniques in order to reduce the number of needed real experiments and improve the quality of approximation models.



[1]Code and dataset to reproduce experiments are available at https://github.com/nx-project/augmentedExperiments

The synthesis of an anticorrosive paint can be achieved by using red pigments from iron ore deposits and the calamine, a recycling of steel by-products. Calamine is formed by high-temperature oxidation during the cooling of products in continuous casting of steels and during heat treatment and hot forming. It is a by-product in different mills (AbedGhars 2018). On the other hand, iron pigments are available in the form of fine dry particles and are soluble in most solvents. Their color is due to their absorption of a part of the wavelengths of the visible spectrum. Online analysis of material properties in metals is a costly and time-consuming problem in industry. Reducing the number of physical experiments is critical. According to some physical characteristics like so-called thermogravimetric analysis (TGA) (see Figure 1a) used as a basic experiment to provide data, we propose a data-driven approach guided by analytical models to predict properties of a mixture of calamine/pigment while reducing the number of needed costly real experiments. First, the signatures of pigment and calamine are established separately. Then, by varying the mixture proportions between calamine and pigment, i.e. the quotient between the weight of pigment and the total charge (weight of calamine plus the weight of pigment), we establish the signature of the new material (See Figure 1b and 1c). Our goal is to provide a model able to predict the material signature for a mixture of pigment and calamine using a minimal number of real experiments. To guide the transformations between physical experiments, we leverage known analytical models such as Arrhenius (Laidler 1984) and Eyring (Eyring 1935) kinetic models which describe the degradation kinetics of chemical reactants.

Combining the aforementioned approved a priori knowledge leads to a hybrid model with fewer degrees of freedom and an improved extrapolation range. This approach forces the model to realize certain conditions/equations that are part of the prior knowledge. For example, a neural network model without modification would have to approximate the mass conservation laws that apply to any chemical conversion. If mass conservation is enforced, the errors associated with this approximation are avoided (Zander, Dittmeyer, and Wagenhuber 1999). Similarly, authors in (Greydanus, Dzamba, and Yosinski 2019) draw inspiration from Hamiltonian mechanics to train models that learn exact conservation laws in an unsupervised manner by endowing the models with better inductive biases.

The aim of incorporating additional forms of supervision has been a popular theme recently in machine learning. For example, a priori knowledge in the form of definite equations is used to pre-structure data-driven models (Zander, Dittmeyer, and Wagenhuber 1999; Overstall, Woods, and Martin 2019). Another way of incorporating a priori knowledge is to enforce fulfillment of certain conditions/equations which are part of the a priori knowledge by constraining the output layer of the models. In this sense, a variety of methods for modifying the learning objective via additional regularization-like terms have been proposed (Tarlow and Zemel 2012; Mann and McCallum 2010; Ganchev et al. 2010; Osmani, Hamidi, and Bouhouche 2019). In (Pathak, Krahenbuhl, and Darrell 2015), authors used a series of additional linear constraints into the cost function for weakly supervised semantic image segmentation. Authors in (Márquez-Neila, Salzmann, and Fua 2017) explored the benefits and limitations of imposing hard constraints on 3D human pose estimation. In (Oktay et al. 2017), prior knowledge about organ shape and location was used in the form of constraints for image segmentation and analysis. The reduced degree of freedom of these kinds of models has a remarkable consequence of reducing the demand for measurement data (Hamidi and Osmani 2020). Similarly, authors in (Stewart and Ermon 2017), for example, proposed a label-free setting where models are supervised by specifying physics-derived constraints that should hold over the output space, rather than direct examples of input-output pairs. The need for regularization terms in these contexts, then, shifts to ensuring that the models do not converge towards trivial solutions.

Our contributions can be summarized as follows. (1) We frame a real-world application of material engineering into a setting under which we seek to reduce the number of real experiments using domain analytical models; (2) we propose a novel approach for incorporating domain analytical models via regularization-like terms. We ensure that we converge to Pareto-optimal solutions using conditional gradient descent; (3) Extensive experimental analysis reveal that using our approach we achieve remarkable efficiency improvement (reducing the number of real experiments while keeping high approximation capability), which we attribute to the use of a combination of analytical models in specific locations of the chemical reaction's state space.

## Application Description

The present work is part of the objective of exploiting the iron scale produced by the iron and steel industry in order to obtain a rust-proof paint pigment. This raw material will be used in a defined proportion mixed with a natural iron oxide pigment. We are mainly interested in the study of their physico-chemical characteristics (AbedGhars 2018), and particularly, thermal and mass loss analysis as shown in Figure 1.

In this section, we introduce some domain-specific notions that are important to understand the rest of the paper. We present the main materials used in our experiments: red pigment and calamine oxide and their mixtures. Then, as the theoretical framework used to control real experiments

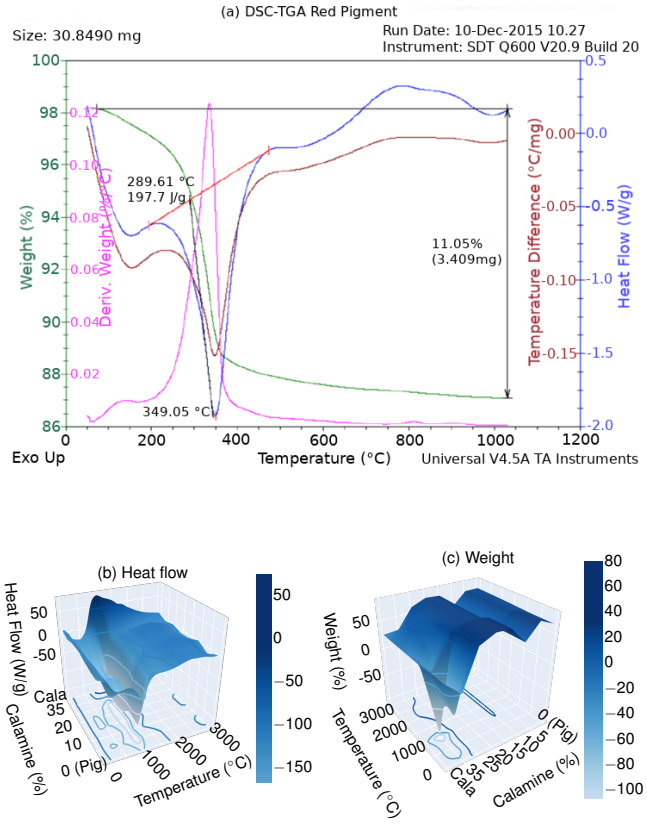


Figure 1: Simultaneous thermal and mass loss analysis of (a) red pigment and (b, c) binary mixture of red pigment and additional calamine percentages. The effect of the temperature augmentation on the behavior of the red pigment is shown via weight, derivative weight, temperature difference, and heat flow curves. Further analysis of mass loss, variation of the dissociation reaction enthalpy, and the formation of new phases can be found in Section Thermal Analysis.

is based on thermal analysis and kinetics models, we will give a short description of both of them.

### Binary Mixture and Target Material

The application goal is to characterize and to synthesize a new paint pigment based on the calamine oxide and red pigment ensuring desired properties at some given temperatures. **Red Pigment** is a natural form of mineral composed mainly of iron oxide; its individual thermal signature is given in Figure 1a. This analysis shows a mass loss which is attributed to the evaporation of water formation of iron hydroxides corresponding to the dissolution of goethite FeO (OH) (AbedGhars, Bouhouche, and Ghers 2017). **Calamine Oxide** is a steel by-product obtained during continuous casting or heating of slabs and billets. This product is not a sterile waste and may have a meaning of raw materials in its own, which can be valued and marketed. The synthesis of new materials is obtained by the contribution of the calamine in this process by ensuring a sufficient quantity of $Fe_2O_3$

and increasing the density of the synthesized pigment (Figures 1b and 1c). In parallel, the goal of this application is to get materials with some desirable qualitative properties including optical properties (the size of the pigment particles may affect the final appearance of the coated surface: a paint can be glossy, matte, or satiny, depending on the particles' size which affect the phenomena of diffusion, reflection, and refraction of light), ferromagnetic properties, etc.

The new material synthesis can be viewed from several theoretical models. Each one uses approved knowledge of the field and predicts the expected theoretical trajectories. The most prominent models that we leverage in our proposed method are **thermal** and **kinetics** models.

## Thermal Analysis

Thermal analysis is a set of techniques used to measure the evolution of physico-chemical quantity of a given material as a function of temperature, time, and atmosphere. These are mainly used in material characterization but also for quality control/assurance and failure analysis in industry. In our case, we focus on the thermogravimetric analysis (TGA) and the differential scanning calorimetry (DSC).

TGA is often used in research and testing to determine the characteristics of materials, such as polymers, in order to estimate the corrosion oxidation kinetics at high temperatures, the degradation temperatures, the moisture absorbed by the material, the amount of organic and inorganic compounds in a material, the decomposition point of an explosive and solvent residues. The DSC signal measures the differences in heat exchange between a sample to be analyzed and a reference. The DSC signal reveals transitions associated with the dehydration, a polymorphic phase transition, and the high-temperature melt.

Our dataset is built from real experiments using the SDT-Q600 version 20.9 thermogravimetric analyzer. Simultaneous thermal and mass loss analysis for calamine oxide shows an increase in weight (3.602%) between 400 and 1000°C, which is attributed to the oxidation reaction of iron oxides (new phase formation) according to the reaction $3\,FeO + \frac{1}{2}\,O_2 \longrightarrow Fe_3O_4$. Between $850\,^{\circ}C$ and $1150\,^{\circ}C$, the system remains stable, according to the reaction $2\,Fe_3O_4 + \frac{1}{2}\,O_2 \longrightarrow 3\,Fe_2O_3$. This oxidation is accompanied by weight gain and heat generation (exothermic reaction) respectively of 3.602% and 1.128 W/g. For iron pigment (Figure 1a), this analysis shows a mass loss which is attributed to the evaporation of water formation of iron hydroxides (goethite FeOOH dissolution). This decrease is 11.05% between temperatures $289\,^{\circ}C$ and $349\,^{\circ}C$. This dissolution is accompanied by absorption of heat (endothermic) equal to 1.926 W/g as shown in Figure 1a. The transformation of $\alpha$FeOOH (goethite) to $\alpha Fe_2O_3$ (hematite) during the heating higher than $255\,^{\circ}C$ is evidenced by a loss of weight during the TGA test. The dehydration mechanism involves the elimination of $H_2O$. Hematite begins to grow starting only from a weight loss of 3.97% when we have the synthetic goethite. The transformation of the product (dehydration) is done starting from the surface towards the inside of the grains by the formation of pores and the release of water vapor.

## Kinetics Models

Kinetic models describe the time evolution of the mass as well as the temperature difference of the analyzed components during the thermal degradation process. The complexity of the chosen model depends on the desired objectives.

The simple method for obtaining kinetic parameters from experimental data is based on the kinetic equation $\frac{\partial \alpha}{\partial t} = k(1-\alpha)^n$, where $\frac{\partial \alpha}{\partial t}$ is the rate of the reaction (or decomposition). The constant $k$ is given by

$$k = Ae^{-E_a/RT} \tag{1}$$

where $A$ is the pre-exponential factor, $E_a$ is the activation energy and $R$ is the gas constant. This is the Arrhenius equation (Laidler 1984) which gives the dependence of the rate constant of a chemical reaction on the absolute temperature and the constants of the reaction.

In our case, we are more interested in the collision theory underlying this model and in particular the pre-exponential factor, which defines the frequency at which molecules collide during a chemical reaction, and its link to the concentrations of each of the considered components in our application. Indeed, we exploit the variations of this parameter and the related kinetic models in order to constrain the machine learning models we build.

Alternatively, the Eyring equation (Eyring 1935) is based on transition state theory (Lasaga 1981) and is used to describe the relationship between reaction rate and temperature. The Eyring equation is defined as follows:

$$k = \frac{k_B T}{h} e^{-\frac{\triangle H^{\ddagger}}{RT}} e^{\frac{\triangle S^{\ddagger}}{R}} \tag{2}$$

where $\Delta H^{\ddagger}$ is the enthalpy of activation, $\Delta S^{\ddagger}$ is the entropy of activation, $k_B$ is Boltzmann's constant, and $h$ is Planck's constant. It is similar to the Arrhenius equation, which also describes the temperature dependence of reaction rates. However, whereas the Arrhenius equation can mainly be applied to gas-phase kinetics, the Eyring equation is useful in the study of gas, condensed, and mixed-phase reactions that have no relevance to the collision model. In addition, the Arrhenius equation is theoretically derived while the Eyring equation is based on empirical evidence. At very high temperatures, the two models diverge significantly: according to the Arrhenius model, the rate approaches an asymptotic value, while according to the Eyring model, it continues to rise (Peleg, Normand, and Corradini 2012).

In our model, the gas-phase kinetics are circumscribed to the regions where the components undergo exothermic reactions (See thermal analysis). In the mixed-phase reactions that appear in the remaining regions, we make use of the Eyring equation in order to constrain the learning process.

# Generative Model for Augmented Experiments

This section summarizes the problem setting and details the model of augmented experiments including the evaluation protocol, machine learning model, and the way domain analytical models are used to constrain the learning phase.

## Problem Setting

Let us consider a dataset $\mathcal{D} = \{\mathcal{X}^1, \ldots, \mathcal{X}^n\}$ consisting of $n$ sets of experiments conducted using a mixture of the red pigment and calamine oxide at a specified calamine percentage $p_i$, $i \in \{1, \ldots, n\}$. All experiments in each set $\mathcal{X}^i$ are carried out in a predefined discrete range of temperature signal $u(t)$ denoted: $t_1, \ldots, t_{max}$. In the case of TGA calcination process, for example, each single experiment $x_j^i \in \mathcal{X}^i$, corresponds to the process of calcination applied to a given mixture of the red pigment and calamine oxide at a specific $p_i$ calamine percentage and at a given temperature $t_j$.

In addition to the percentage $p_i$ at which an experiment is conducted, it is described by various scalar measures captured via different sensors which characterize the obtained state of the system after applying the process of calcination. The result of an experiment is referred to as a state of the chemical reaction and is described (characterized) by what we call state variables. The main state variables captured via TGA include heat flow, sample purge flow, temperature of the mixture, and mass of the mixture. In our setting, for each experiment $x_j^i$, we consider two important parameters: the temperature and mass, as a function of the mixing percentage $p_i$ of calamine for temperature value $t_j$.

We assume that within the regions where our model generates augmented experiments the phase transitions in the new mixtures of the red pigment and calamine oxide are those detected in each element of the mixture individually. The set of all experimental results obtained for every mixture percentage and every temperature input form what we refer to as the state space.

## Machine Learning Model

In order to train a given architecture, we frame the reconstruction of the state variables as a regression problem, where the goal is to learn a function $f : X \rightarrow Y$ mapping inputs to outputs. As in the traditional regression setting, performance of a learning model is quantified with a loss function, $\mathcal{L}$, and a mapping is found via

$$f^* = \underset{f \in \mathcal{F}}{\operatorname{argmin}} \, \mathcal{L}(f) \tag{3}$$

which can be optimized using a gradient descent algorithm over a pre-defined class of functions $\mathcal{F}$. In our case, $\mathcal{F}$ will be neural networks parametrized by their weights and the loss function will be $\mathcal{L}(f) = \frac{1}{2N} \sum_{i=1}^{N} (f(\mathbf{x}_i) - y_i)^2$, where $N$ is the number of training examples. For a fixed architecture, i.e., a particular instantiation of the hyperparameters, the optimization process will tune the weights of the network and, by the same occasion, the subsequent uni-modal and multi-modal features extracted from the input signals.

## Evaluation Protocol

As mentioned above, the goal is to recover the state space using subsets of the real experiments conducted at particular percentages of the calamine oxide composing the mixtures. To overcome the inherent challenges, we propose to frame the recovering of the state space from an evaluation protocol point of view, where one has to select, accordingly, the appropriate sets of real experiments or individual windows of experiments to feed a machine learning model. Figure 2 illustrates a representation of the state space and its subdivision into partitions.

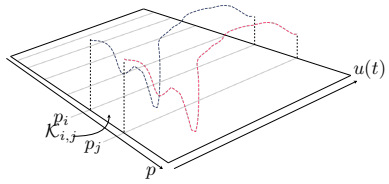


Figure 2: Representation of the state space and the subdivision into partitions $\mathcal{K}_{i,j}$, $i \in \{1, n-1\}$, delimited by the sets of experiments $\mathcal{X}^i$ and $\mathcal{X}^j$ conducted at $p_i$ and $p_j$ percentages of additional calamine oxide, respectively.

Using the $n$ sequences of real experiments $\mathcal{X}^i$ ($i \in \{1, n\}$), given in the dataset $\mathcal{D}$ described previously, ordered by the percentage $p_i$ ($i \in \{1, n\}$) of calamine in the mixture, we divide the state space into $n-1$ contiguous partitions, $\mathcal{K}_i$ with $i \in \{1, n-1\}$ such that $\forall i \in \{1, n-1\}$, $p_i < p_{i+1}$. Also, we define a partition with the percentage of calamine greater than $p_j$ but obtained by the extension of the model between two sets of real experiments $\mathcal{X}^i$ and $\mathcal{X}^j$. We denote this partition $\mathcal{K}_{i,j}$ ($i, j \in \{1, n\}$ and $i < j$).

As a result, we consider two kinds of machine learning models: (1) a model that approximates experiments in the partition $\mathcal{K}_{i,j}$ circumscribed by two given sets training experiments; (2) a model that approximates experiments for the partition beyond a fixed partition $\mathcal{K}_i$.

**Recovering inside circumscribed regions.** In this configuration, we try to recover the partition $\mathcal{K}_{i,j}$ from its delimiting sets of experiments $\mathcal{X}^i$ and $\mathcal{X}^j$. For this we train a model $\mathcal{M}_{\mathcal{K}_{i,j}}$ using all elements of these two sets and we perform validation on the set of experiments $\mathcal{X}^k$, with $i \leq k \leq j$.

**Recovering outside a circumscribed region.** In this configuration, we use sets of experiments $\mathcal{X}^i$ in order to recover partitions $\mathcal{K}_k$ that fall outside the sets of experiments conducted with $\mathcal{X}^i$. In this case, we train a model $\mathcal{M}_{\mathcal{K}_i}^k$ using all elements of partitions labeled by $j$ such that $j <= i$ and we perform validation on the set of experiments $\mathcal{X}^k$ such that $k > i$. Here, we want to assess the ability of these models to extrapolate to other partitions and to what extent they can do that.

## Kinetic-Based Regularization

As we move far away from the set of real experiments or increase the distance between them, reconstruction models based exclusively on the real experiments tend to be very unstable. In these regions, real experiments alone are not sufficient to satisfactorily determine the values of the state variables. In order to account for this instability, we instrument our approach with the set of kinetics models described in Section **Kinetics Models**.

Here, we combine the kinetic models via regularization. Our aim is not to reduce model complexity but leverage regularization as a mean for incorporating additional forms of supervision: in our case, kinetic-based models. This additional regularization-like term is derived from the kinetic models and allows the trained models to stay in a theoretically bounded range. We derive from these models an additional term, $R : \mathcal{F} \rightarrow \mathbb{R}$, that is plugged to the original optimization objective (Equation 3), which, then, becomes:

$$f^* = \underset{f \in \mathcal{F}}{\operatorname{argmin}} \mathcal{L}(f) + \lambda R(f) \tag{4}$$

where $\lambda \in ]0; 1]$ is a weight parameter used to control the impact of the regularization term. This term is used precisely at the interfaces between the various sets of experiments $\mathcal{X}^i$ that partition the state space. By adding this regularization term to the standard loss function (Equation 3), the model considers both the mean squared differences between model prediction and real experiments as well as the divergence from the governing kinetics models (as reflected by the second term in Equation 4).

We leverage the pre-exponential factor and its variations for small increments $\Delta p$ of the percentage of the two components in the mixture. Additional concentrations of some components imply more molecules collisions and thus an increase in the pre-exponential factor. We compute numerically the pre-exponential factor for these small variations and use them to encode the desire for the continuity of state variables values for variations of the mixture percentage.

At any given calamine percentage $p_i$, we compute numerically the kinetic constant $k$ which defines the kinetic energy of the reactants. This allows us to derive a series of penalty bounds $\mathbf{b}_j = [\Delta_j^{t_1}, \ldots, \Delta_j^{t_{max}}]$ at each applied temperature $t_1, \ldots, t_{max}$ using the neighboring points $p_i + \Delta p$, $p_i + 2\Delta p$, $p_i + 3\Delta p$, and so on. The regularization-like term becomes

$$R(f) = \frac{1}{P} \sum_{j=1}^{P} \mathbb{1}\{|f(p_i + j\Delta p) - \mathbf{b}_j| > \epsilon\} \tag{5}$$

where $P$ is the number of neighboring points and depends on both the distance between the sets of experiments and the extent of the small increments $\Delta p$. This additional term provides a necessary constraint, which our model must satisfy. We thus push our model in the direction of better satisfying both terms of the cost function.

**Finding Pareto-optimal solutions.** Within the framework of our application (and of the approximation capacities that we are targeting), the regularization-like term that we graft on the cost function (Equation 4) is essential in order to force the model to take into account the continuum between the different $p_i$, and thus obtain optimal solutions. However, during the optimization process, convergence towards a solution satisfying both terms of the equation simultaneously is not ensured. The optimality criterion for us corresponds to finding so-called Pareto-optimal solutions such that none of $\mathcal{L}(f)$ or $R(f)$ can be made better without making the other worse. Using the Langrangian interpretation, Equation 4 is the same as the following constrained formulation,

$$f^* = \underset{f \in \mathcal{F}}{\operatorname{argmin}} \mathcal{L}(f) \text{ s.t. } R(f) \leq \mu \tag{6}$$

where the soft-constraint problem of Equation 4 becomes a hard-constraint one. Recent advances in neural networks optimization demonstrated noticeable successes in many fields using conditional gradient (CG) which leads to Pareto-optimal solutions and eventually to improved generalization (Ravi et al. 2019). Indeed, formulation (Equation 4) falls under the category of "scalarization" technique whereas (Equation 6) is $\epsilon$-constrained technique. It is known that when the problem is non-convex, $\epsilon$-constrained technique yields Pareto-optimal solutions whereas scalarization technique does not (Boyd and Vandenberghe 2004; Ravi et al. 2019). We ensure the fulfillment of the additional derived constraints using CG where gradient steps rely on a linear minimization oracle over the set of constraints defined by the additional regularization term.

## Experiments

In this section, we evaluate our approach on a real industrial application dataset and demonstrate how it can reliably reconstruct the state space of the experiments using various configurations combining real experiments and analytical models. All of our experiments are implemented using Tensorflow framework (Abadi et al. 2016) and the following describes the details of experiments and obtained results. Code to reproduce experiments is publicly available at https://github.com/nx-project/augmentedExperiments.

**Dataset description.** Dataset consists of thermal analysis of raw materials. These were collected with an SDT-Q600 industrial instrument that monitors the calcination of the mixtures continuously. The instrument encompasses a pair of thermocouples within the ceramic beams that provides direct sample, reference, and differential temperature measurements from ambient to 1500 °C (using a ramp of 40 °C/min). Specifically, various signals are monitored by the instrument, including, weight (mg), heat flow (mW), temperature difference ($\mu V$), sample purge flow (mL/min), etc. The dynamics of the Nitrogen gas, which constitutes the ambient atmosphere around the mixture, is set to 100 ml/min. The acquisition of the various signals was carried at a sampling rate of 2 Hz which is sensitive enough, in these kinds of applications, for capturing temperature and mass trends which may indicate regime changes. In total, 3000 measurement points were obtained for each set of experiments. In addition to the theoretical curves of the red pigment ($pig$) and the calamine oxide ($cala$) that were obtained separately, we perform calcination of mixtures with various percentages, $p_i \in \{5, 10, 15, 20, 25, 35\}$, of additional calamine oxide.

**Training details.** We construct neural networks by stacking 3 Fully Connected/ReLU layers with dropout probability 0.5 and two regression outputs (for weight and temperature). We optimize the neural architectures, including the number of neurons in each layer, using Bayesian optimization (Snoek, Larochelle, and Adams 2012) (The complete

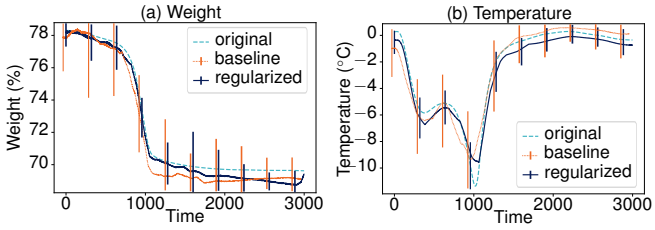


Figure 3: Obtained state space reconstructions for (a) weight and (b) temperature. We report reconstructions averaged over all evaluation setups and their corresponding perplexity. As references, we also report the reconstructions obtained (under the same evaluation setups) using the baseline.

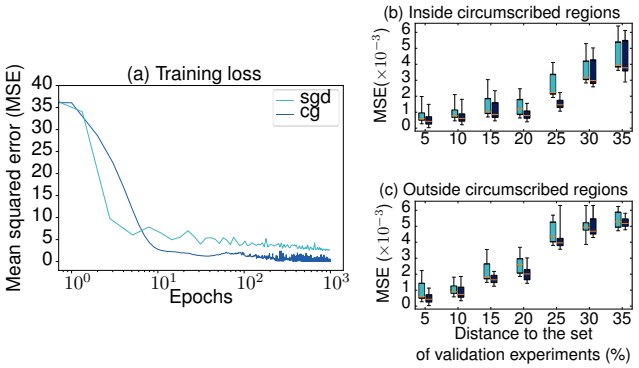


Figure 4: Comparing the performances of SGD vs. CG: (a) evolution of the training loss as a function of the number of training epochs; (b and c) extent of the reconstructions as a function of the distance from the set of training to the set of validation experiments (inside and outside circumscribed regions of the state space, respectively). We repeat the evaluation for 10 times with different random seeds and report the median and the best validation performance of the models.

list of hyperparameters and their range of values can be found in the code repository). The networks are trained for 1000 epochs on the training data and evaluated on the test set. The learning rate is set to 0.0001. We perform train-test splits over different runs by stratifying the learning examples. The model is trained to reconstruct the weight and the temperature state variables simultaneously by minimizing the mean squared loss between the original target signal and the reconstruction provided by the network. In the case of SGD, weights of the neural network are optimized using the Adam algorithm (Kingma and Ba 2014). As a reference, we also train a model (referred to as baseline) using the same evaluation setup and a comparable number of parameters but without any additional derived constraint.

## Evaluation of the Reconstruction Process

In our first set of experiments, (1) we evaluate the reconstructions obtained using different configurations of the real experiments based on the setting described in Section **Evaluation Protocol**; (2) we assess the extent of reconstructions as a function of the distance to the set of validation experiments and the impact of using CG on the fulfillment of the additional constraints; (3) we evaluate the reconstruction performances at specific percentages of additional calamine.

Figures 3a and 3b show the obtained state space reconstructions of weight and temperature, respectively. Obtained reconstructions are averaged over all evaluation settings. We additionally report their corresponding perplexity. These two figures highlight in particular the perplexity of the naive approach (baseline). Our approach contributes to a substantial reduction of this perplexity (e.g. $2.76\pm0.09$ vs $3.29\pm0.15$ for weight; 55.7 vs 59.4 for temperature). The perplexity here can be related to 2 factors: the spacing of the real experiments; and the presence of phase transitions especially in the range [250; 1250] for temperature. To verify the impact of experiment spacing, we measure the extent of reconstructions as a function of the distance from the set of training to the set of validation experiments. We provide numerical evidence in Figure 4 with the evaluation protocol defined above. We repeated the evaluation setup for 10 times. We can see that until 20%, both inside and outside circumscribed regions, our approach provides controlled perplexity.

Furthermore, Figure 4 illustrates also the impact of using CG on the fulfillment of the constraints that are imposed on the models. We can see a noticeable effect of CG on the reconstruction performances up to an extent of 25% (Figure 4b) and 30% (Figure 4c). This translates the ability of CG to converge towards solutions that take into account the regularization-like terms whereas SGD tends to push towards solely satisfying the first term of the cost function at the expense of providing constrained reconstructions. After that extent, we can notice that performances of CG and SGD are comparable for models trying to extrapolate far away from the real experiments. This could be explained by the fact that the penalty bounds are becoming loose from that point, which does not help the model to reconstruct correctly. Despite the existence of many phase transitions that span all over the state space, our approach is particularly able to reconstruct the weight and temperature states. Even when we reduce the number of real experimental points, the obtained reconstruction quality remains high.

We further investigate the extent of reconstructions at specific percentages of additional calamine oxide. We report the average reconstruction performances over all configurations of the sets of training experiments. It is worth noticing that for some percentages, e.g. reconstructions of temperature curves at 15%, no matter how far apart the set of training experiments are, the reconstructions are satisfactory with or without the addition of analytical models. However, the analytical models contribute substantially to reducing the accompanied perplexity ($0.00192\pm.00081$ vs. $0.0076\pm.0023$). On the other hand, for 35% for example, the reconstruction errors are greater using the baseline model. This could also be explained by the numerous phase transitions that exist around this percentage. In this case, our approach is able to significantly improve upon the baseline model and overall in all percentages both in terms of approximation and per-

| Analytical model(s) | Reconstruction error avg.±std. $\times 10^{-2}$ (best extent %) | | | |
|---|---|---|---|---|
| | $\lambda = 0.001$ | $\lambda = 0.01$ | $\lambda = 0.1$ | $\lambda = 1$ |
| Arrhenius (A) | 0.933 ± .0073 (5) | 0.988 ± .0023 (15) | **0.39 ± .0157** (15) | 0.776 ± .0027 (5) |
| Eyring (E) | 0.57 ± .0145 (10) | 0.385 ± .0031 (5) | **0.228 ± .0079** (10) | 0.587 ± .0037 (**20**) |
| *pig* (P) | 2.408 ± .0034 (10) | **0.408 ± .015** (5) | 1.188 ± .0061 (5) | 2.408 ± .0042 (10) |
| *cala* (C) | 0.533 ± .0112 (15) | 0.512 ± .0055 (**20**) | 0.524 ± .0047 (5) | **0.504 ± .0125** (10) |
| A+E | **0.188 ± .0058** (5) | 0.197 ± .0079 (**20**) | 0.214 ± .0051 (10) | 0.204 ± .0147 (15) |
| P+C | 0.318 ± .0012 (5) | **0.289 ± .0044** (10) | 0.309 ± .0108 (10) | 0.320 ± .0086 (10) |
| A+E+P+C | **0.192 ± .0056** (15) | 0.201 ± .0122 (5) | 0.247 ± .0032 (10) | 0.231 ± .0143 (15) |

Table 1: Summary of the reconstruction errors obtained via kinetic-based regularization. We evaluated various domain analytical models and different values for the parameter $\lambda \in \{0.001, 0.01, 0.1, 1\}$ which controls the impact of the regularization-like term. Results averaged over all possible percentages of additional calamine and evaluation configurations.

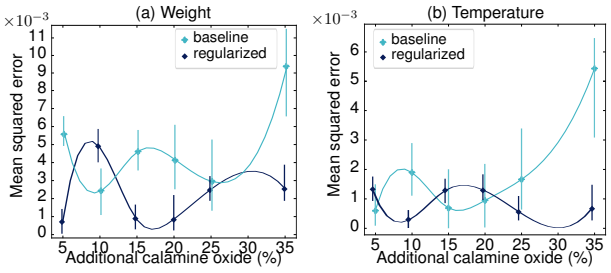


Figure 5: Reconstruction performances at specific percentages of additional calamine oxide. We compare the reconstructions, of (a) weight and (b) temperature, obtained using the baseline vs. the regularized models. Results averaged over all possible distances to the set of training experiments.

plexity (e.g. 0.00087±.00122 vs. 0.00477±.0021 at 15%; 0.00246±.002 vs. 0.00932±.0056 at 35%).

## Trade-off between Real Experiments and Richness of the Domain Models

In the previous experiments, we showed the ability of our approach to reconstruct precisely both the portions of the state space delimited by and those falling outside sets of experiments. Here, we evaluate the trade-off between richness of the domain analytical models, which are plugged to the optimization objective of the learning models via regularization, and the granularity of real experiments.

For this, we compare reconstruction models trained using different configurations of the kinetic and thermal-based regularization-like terms. Precisely, we use the *Arrhenius* and *Eyring* models, as well as the theoretical curves, *pig* and *cala*, to derive these terms. We distinguish a first configuration where the analytical models are each plugged individually to guide the learning models and a second configuration where we combine them together, i.e., *Arrhenius* and *Eyring* models (A+E), *pig* and *cala* (P+C), and all these models combined together (A+E+P+C). Additionally, we provide the best extent of reconstruction (in %) that was achieved in each configuration. Table 1 summarizes the obtained results.

In both configurations, the analytical models improve significantly the performances of the reconstructions generated by the learning models. Very interestingly, using the theoretical curve of the red pigment, the constructed models are able to get a substantial gain in terms of reconstruction losses. In particular, for $\lambda = 0.01$, we obtain an improvement factor of 10 over the remaining values of $\lambda$ of the same configuration. On the other hand, the models guided by the theoretical curve of the calamine outperform those guided by the red pigment (except for $\lambda = 0.01$, but there the difference is smaller than for the other values of $\lambda$). This observation shows that some analytical models are more adapted than others, which is further confirmed when we compare the influence of the *Arrhenius* and *Eyring* models on the generated reconstructions. Besides, we can observe that models guided by a combination of A+E outperform both A+E+P+C and, by far, P+C, while attaining a reconstruction extent of over 20%.

Overall, these combinations have better reconstruction performances than the baseline or analytical models taken individually since their impact is adapted to different regions of the state space. These results give additional insights into the study of trade-offs between the richness and complexity of domain analytical models and the amount of real experimental data (or sensor measurements in the case of real sensors) needed to train learning models.

## Conclusion

To reduce the number of costly real experiments in industrial applications, we proposed a machine learning approach guided by theoretical domain models and a minimum number of additional constraints to generate new experiments with controlled approximation quality. In our practical case, we generate synthesis materials to discover new anticorrosive paints under the constraint stating that the only phase transitions in the mixtures are those existing in each material. Intensive experiments show that our model which combines the principle of thermogravimetric analysis and machine learning is able to augment the real experiments to significant extents. Even if the proposed evaluation protocol reduces the number of required experiments, we plan to include in future versions of the model additional theoretical models to overcome the prediction approximation.

## References


Abadi, M.; Barham, P.; Chen, J.; Chen, Z.; Davis, A.; Dean, J.; Devin, M.; Ghemawat, S.; Irving, G.; Isard, M.; et al. 2016. Tensorflow: A system for large-scale machine learning. In *12th USENIX Symposium on Operating Systems Design and Implementation (OSDI 16)*, 265–283.

AbedGhars, M. T. 2018. *Contribution à la caractérisation et synthèse de pigment de peinture à base de calamine. Evaluation de la qualité et analyse des incertitudes sur les propriétés.* Ph.D. thesis, Université Badji Mokhtar de Annaba.

AbedGhars, M. T.; Bouhouche, S.; and Ghers, M. 2017. Prediction of thermal and mass loss behavior of mineral mixture using inferential stochastic modeling and thermal analysis measurement data. *Measurement* 109: 326–333.

Aykol, M.; Hegde, V. I.; Hung, L.; Suram, S.; Herring, P.; Wolverton, C.; and Hummelshøj, J. S. 2019. Network analysis of synthesizable materials discovery. *Nature communications* 10(1): 2018.

Biegler, L. T.; Lang, Y.; and Lin, W. 2014. Multi-scale optimization for process systems engineering. *Computers & Chemical Engineering* 60: 17–30.

Boyd, S. P.; and Vandenberghe, L. 2004. *Convex optimization*. Cambridge university press.

Eyring, H. 1935. The activated complex in chemical reactions. *Journal of Chemical Physics* 3(2): 107–115.

Ganchev, K.; Graça, J.; Gillenwater, J.; and Taskar, B. 2010. Posterior regularization for structured latent variable models. *Journal of Machine Learning Research* 11: 2001–2049.

Greydanus, S.; Dzamba, M.; and Yosinski, J. 2019. Hamiltonian neural networks. In *Advances in Neural Information Processing Systems*, 15379–15389.

Hamidi, M.; and Osmani, A. 2020. Data Generation Process Modeling for Activity Recognition. In *European Conference on Machine Learning and Principles and Practice of Knowledge Discovery in Databases*. Springer.

Kingma, D. P.; and Ba, J. 2014. Adam: A method for stochastic optimization. *arXiv preprint arXiv:1412.6980* .

Laidler, K. J. 1984. The development of the Arrhenius equation. *Journal of Chemical Education* 61(6): 494.

Lasaga, A. C. 1981. Transition state theory. *Rev. Mineral.* 8.

Li, J.; and Stoliarov, S. I. 2013. Measurement of kinetics and thermodynamics of the thermal degradation for non-charring polymers. *Combustion and Flame* 160(7): 1287–1297.

Mann, G. S.; and McCallum, A. 2010. Generalized Expectation Criteria for Semi-Supervised Learning with Weakly Labeled Data. *Journal of Machine Learning Research* 11(2): 955–984.

Márquez-Neila, P.; Salzmann, M.; and Fua, P. 2017. Imposing hard constraints on deep networks: Promises and limitations. *arXiv preprint arXiv:1706.02025* .

Oktay, O.; Ferrante, E.; Kamnitsas, K.; Heinrich, M.; Bai, W.; Caballero, J.; Cook, S. A.; De Marvao, A.; Dawes, T.; O'Regan, D. P.; et al. 2017. Anatomically constrained neural networks (ACNNs): application to cardiac image enhancement and segmentation. *IEEE Transactions on Medical Imaging* 37(2): 384–395.

Osmani, A.; Hamidi, M.; and Bouhouche, S. 2019. Monitoring of a Dynamical System Based on Autoencoders. In *proceedings of the 28th International Joint Conference on Artificial Intelligence, IJCAI*, 1836–1843.

Overstall, A. M.; Woods, D. C.; and Martin, K. J. 2019. Bayesian prediction for physical models with application to the optimization of the synthesis of pharmaceutical products using chemical kinetics. *Computational Statistics & Data Analysis* 132: 126–142.

Pathak, D.; Krahenbuhl, P.; and Darrell, T. 2015. Constrained convolutional neural networks for weakly supervised segmentation. In *Proceedings of the IEEE International Conference on Computer Vision*, 1796–1804.

Peleg, M.; Normand, M. D.; and Corradini, M. G. 2012. The Arrhenius equation revisited. *Critical Reviews in Food Science and Nutrition* 52(9): 830–851.

Ravi, S. N.; Dinh, T.; Lokhande, V. S.; and Singh, V. 2019. Explicitly imposing constraints in deep networks via conditional gradients gives improved generalization and faster convergence. In *Proceedings of the AAAI Conference on Artificial Intelligence*, volume 33, 4772–4779.

Severson, K. A.; Attia, P. M.; Jin, N.; Perkins, N.; Jiang, B.; Yang, Z.; Chen, M. H.; Aykol, M.; Herring, P. K.; Fraggedakis, D.; et al. 2019. Data-driven prediction of battery cycle life before capacity degradation. *Nature Energy* 4(5): 383.

Snoek, J.; Larochelle, H.; and Adams, R. P. 2012. Practical bayesian optimization of machine learning algorithms. In *Advances in Neural Information Processing Systems*, 2951–2959.

Stewart, R.; and Ermon, S. 2017. Label-free supervision of neural networks with physics and domain knowledge. In *Proceedings of the AAAI Conference on Artificial Intelligence*, volume 1, 2576–2582.

Tabor, D. P.; Roch, L. M.; Saikin, S. K.; Kreisbeck, C.; Sheberla, D.; Montoya, J. H.; Dwaraknath, S.; Aykol, M.; Ortiz, C.; Tribukait, H.; et al. 2018. Accelerating the discovery of materials for clean energy in the era of smart automation. *Nature Reviews Materials* 3(5): 5.

Tarlow, D.; and Zemel, R. 2012. Structured Output Learning with High Order Loss Functions. In *Proceedings of the International Conference on Artificial Intelligence and Statistics*, volume 22, 1212–1220.

Zander, H.-J.; Dittmeyer, R.; and Wagenhuber, J. 1999. Dynamic modeling of chemical reaction systems with neural networks and hybrid models. *Chemical Engineering & Technology: Industrial Chemistry-Plant Equipment-Process Engineering-Biotechnology* 22(7): 571–574.